Strong-coupling phonon-mediated scenario of superconductivity in $Ca_3Ir_4Sn_{13}$ and $Ca_3(Ir_{0.91}Co_{0.09})_4Sn_{13}$

Jianqiang Hou, Chi Ho Wong, and Rolf Lortz*
Department of Physics, The Hong Kong University of Science and Technology, Clear Water Bay, Kowloon, Hong Kong

Romain Sibille and Michel Kenzelmann
Laboratory for Scientific Developments and Novel Materials, Paul Scherrer Institute, CH-5232 Villigen-PSI, Switzerland
(Received 13 July 2015; revised manuscript received 2 March 2016; published 12 April 2016)

We report measurements of the specific heat and electrical resistivity of $Ca_3(Ir_{0.91}Co_{0.09})_4Sn_{13}$ in comparison to $Ca_3Ir_4Sn_{13}$. The Co substitution was chosen to suppress the structural anomaly $T^* = 38$ K reported in $Ca_3Ir_4Sn_{13}$. While the superconducting transition temperature of $Ca_3(Ir_{0.91}Co_{0.09})_4Sn_{13}$ is slightly higher than in the stoichiometric parent compound $Ca_3Ir_4Sn_{13}$, and it displays a stronger superconducting coupling strength, the absence of a structural phase transition allows us to determine the spectral distribution of phonon states and its relation to superconductivity. The phonon density of states $F(\omega)$ and the spectral electron-phonon scattering function ${a_{tr}}^2F(\omega)$ are determined by deconvolution of the specific heat and electrical resistivity, respectively. A dominant mode appears in both histograms at $\hbar\omega = 12$ meV, which indicates that this phonon mode is responsible for the superconductivity in $Ca_3(Ir_{0.91}Co_{0.09})_4Sn_{13}$. The data suggest that superconductivity in this material class can be conclusively explained within a conventional strong -coupling phonon-mediated scenario.

DOI: 10.1103/PhysRevB.93.134505

I. INTRODUCTION

The superconducting pairing mechanism is one of the most important topics of research on superconductors. In conventional superconductors, the electron-phonon interaction is generally believed to be the source of Cooper pairing. However, in many unconventional superconductors, spin fluctuations in the vicinity where a magnetic order is suppressed to zero by a control parameter such as ion substitution or hydrostatic pressure are considered to be of particular importance in the pairing mechanism [1–3]. Antiferromagnetic or ferromagnetic spin fluctuations could result in a nodal superconducting gap (for example, the d-wave gap in cuprates or the p-wave gap in Sr_2RuO_4), while the gap in a conventional superconductor is nodeless [4–6]. Unconventional superconductivity is also sometimes found in the vicinity of the point where charge-density-wave (CDW) instabilities are suppressed by such a control parameter [7]. The latter is a form of electronic order which usually competes with superconductivity.

$Ca_3Ir_4Sn_{13}$ has a cubic structure of space group $Pm\bar{3}n$ [8,9] at room temperature, and was first synthesized 30 years ago with a superconducting transition temperature of about 7 K [10,11]. Few properties had been investigated, until recent detailed experiments revealed that there is a distinct structural transition anomaly at $T^* \cong 38$ K observable in the electrical resistivity and magnetic susceptibility [8], which was proposed to be a transition from a $Pm\bar{3}n$ to a $I\bar{4}3d$ structure based on x-ray diffraction experiments [12]. More recent inelastic neutron scattering experiments in combination with density functional theory suggested that the structural transition arises from the softening of a low-energy phonon mode, which is associated with a "breathing" mode of the Sn_{12} icosahedra [13]. The structural transition T^* can be suppressed by application of chemical or physical pressure [12], which is associated with an increase of the superconducting critical temperature T_c. The phase diagram features a dome of superconductivity in the vicinity of the suppression of the phase transition—not dissimilar to the superconducting dome in the high-T_c superconducting cuprates. In fact, Yang *et al.* had proposed that the presence of this transition may indicate the coexistence of ferromagnetic spin fluctuations and superconductivity [8], thus suggesting an unconventional superconducting mechanism. However, further studies on $Ca_3Ir_4Sn_{13}$, including Seebeck coefficient [14], electrical magnetotransport [15], specific-heat [14], thermal transport [16], and muon spin rotation (μSR) measurements [9,14], all indicated that the superconducting gap of $Ca_3Ir_4Sn_{13}$ is nodeless. In particular, the μSR experiment proved unambiguously that the anomaly at around 38 K is not of magnetic origin [9,14].

It was argued that the structural transition at T^* is the onset of CDW order [12], suggesting that the charge fluctuations associated with the charge order may be involved in the formation of the superconducting phase. Recently, an opening of a gap in the electronic structure was reported, and a decrease of the electronic density of states at the Fermi level by 30% [17]. The observed gap was unexpectedly large compared to the putative CDW transition, which would mean that the CDW is in an extreme strong-coupling limit. Therefore, the role of charge fluctuations and the nature of superconductivity are not well understood in this material.

Klintberg *et al.* provided evidence that $Sr_{3-x}Ca_xIr_4Sn_{13}$ can be tuned through a quantum critical point using hydrostatic pressure [12]. They showed that this quantum critical point involves a structural phase transition at zero temperature. In order to study the series in vicinity to the point where the T^* anomaly is suppressed by an external control parameter at ambient pressure, we substituted iridium for cobalt. For light cobalt substitution we have observed an increase of T_c and a decrease of T^*. Therefore the $Ca_3(Ir_{1-x}Co_x)_4Sn_{13}$ substitution

*Corresponding author: lortz@ust.hk

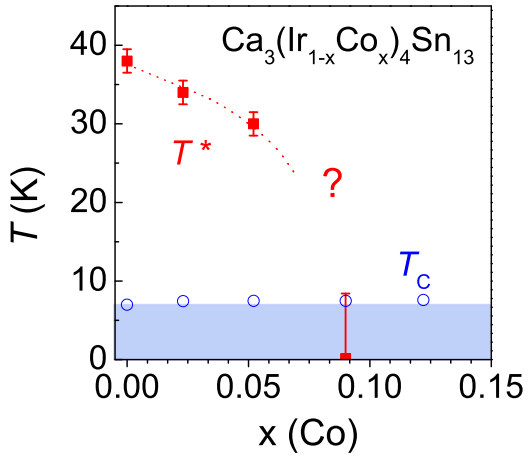

FIG. 1. The evolution of T^* and T_c in $Ca_3(Ir_{1-x}Co_x)_4Sn_{13}$ as a function of Co content x. The dotted line serves as a guide to the eye.

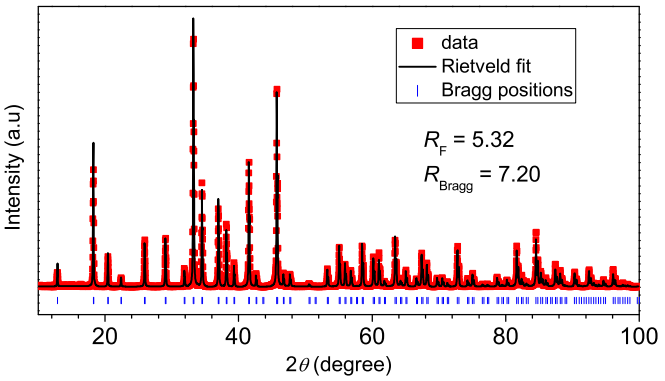

FIG. 2. Rietveld fit of the powder x-ray diffraction data of the $Ca_3(Ir_{0.91}Co_{0.09})_4Sn_{13}$ sample used in this study.

series as a function of Co content x increasingly suppresses the T^* transition and appears to have a similar effect to hydrostatic pressure (see Fig. 1) [18].

In this paper, we report specific-heat and electrical resistivity data of a cobalt-substituted $Ca_3(Ir_{0.91}Co_{0.09})_4Sn_{13}$ single crystal in comparison to a $Ca_3Ir_4Sn_{13}$ single crystal. The specific heat provides evidence for strong-coupling superconductivity, which is slightly enhanced in the Co-substituted sample, in accordance with its higher T_c. We use a deconvolution technique for the analysis of the specific heat and resistivity of $Ca_3(Ir_{0.91}Co_{0.09})_4Sn_{13}$ into a series of Einstein modes and Bloch-Grüneisen modes with different frequencies, respectively. This allows us to investigate the electron-phonon interaction in this material in detail. We find that the lattice specific heat is dominated by a narrow group of phonon modes peaking at ∼12 meV. These phonons show a strong electron-phonon coupling and thus most likely play an important role for superconductivity. Our analysis can conclusively explain superconductivity by a conventional phonon-mediated pairing mechanism in this class of superconductors within a strong-coupling scenario, and thus confirms and complements recent research on these superconducting quasiskutterdites that suggests a complex interplay between soft phonon modes related to a structural instability and strong-coupling superconductivity [19,20].

II. EXPERIMENT

Single-crystalline samples were synthesized using a tin self-flux method. High-purity elements with atomic parts of 3 Ca (Aldrich, 99.99%), 2.2 Ir (Chempur, 99.9+%), 1.8 Co (Aldrich, 99.9+%), and 90 Sn (Chempur, 99.999%) were heated up to 1050 °C in an evacuated and sealed quartz tube. After 2 h at that temperature, the liquid was cooled to 500 °C with a cooling rate of 3 °C per hour and then quenched to room temperature. The excess tin flux was removed using diluted HCl. Large single crystals with dimensions up to several millimeters were obtained. Although the starting mixture corresponded to a target compound of general formula $Ca_3(Ir_{1-x}Co_x)_4Sn_{13}$ with a nominal composition $x = 0.45$, it was established from the powder x-ray diffraction measurement of the lattice constant that the final composition was $x = 0.088(6)$. This was done assuming a Vegard's law between the two end members of the solid solution. The composition obtained by this method was confirmed using spatially resolved micro-x-ray fluorescence measurements (beam size of 30 μm). In addition, $Ca_3(Ir_{1-x}Co_x)_4Sn_{13}$ crystals were grown for several compositions x up to ∼0.12 and it was clear that the final Co content of the crystals was always markedly smaller than that of the starting melt. This indicates a higher affinity of Ir than Co for the 3-4-13 structure in the present synthesis conditions. The Rietveld fit of the powder x-ray diffraction data of the sample used in the present study is shown in Fig. 2.

The dc resistivity ρ was measured with a standard four-probe technique from 1.8 to 300 K with current reversal using conducting silver paint for the contacts. The specific heat C at constant pressure was measured using a high-precision continuous-heating adiabatic calorimeter at high temperature from 50 to 300 K, combined with a generalized long relaxation technique in the low-temperature regime between 1.8 and 50 K.

III. RESULTS AND DISCUSSION

The resistivity of $Ca_3(Ir_{0.91}Co_{0.09})_4Sn_{13}$ in comparison to $Ca_3Ir_4Sn_{13}$ is shown in Fig. 3. The residual resistivity $\rho_0 = 25.6\,\mu\Omega$ cm of $Ca_3(Ir_{0.91}Co_{0.09})_4Sn_{13}$ will be required for our analysis of the normal-state properties later and is determined by extrapolating the resistivity data in the normal state to zero temperature. The anomalous broad hump at $T^* = 38$ K is visible in the $Ca_3Ir_4Sn_{13}$ data, but appears to be entirely suppressed in the resistivity data of $Ca_3(Ir_{0.91}Co_{0.09})_4Sn_{13}$. The latter material can thus serve us as a sample without T^*, which is crucial for our data analysis. The superconducting transition temperature of the $Ca_3(Ir_{0.91}Co_{0.09})_4Sn_{13}$ sample is $T_c = 7.5$ K, as obtained from the midpoint of the resistivity jump, which is slightly higher than the $T_c = 7.0$ K of $Ca_3Ir_4Sn_{13}$. The values of T^* and T_c in the composition range that we have explored up to $x \sim 0.12$, are summarized in Fig. 1.

The specific-heat data is shown in Fig. 4. The temperature range in our measurement extends from 1.8 K up to 300 K. Figure 4(a) presents the specific heat of $Ca_3Ir_4Sn_{13}$. The jump at 6.8 K in the C/T vs T curve indicates the superconducting transition temperature of $Ca_3Ir_4Sn_{13}$. The anomaly $T^* = 38$ K

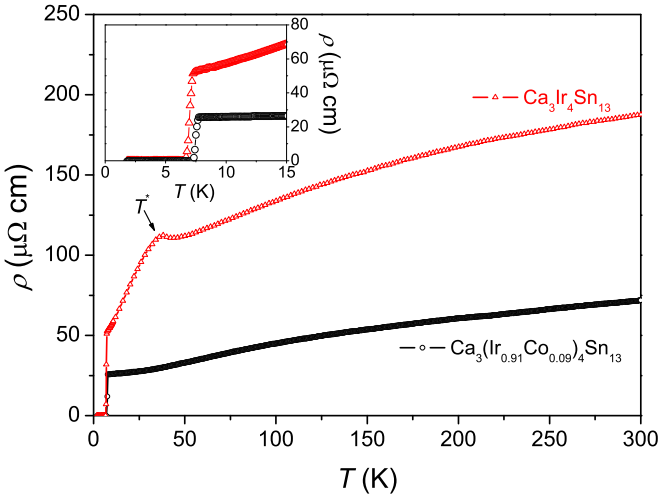

FIG. 3. Temperature dependence of the electrical resistivity of $Ca_3(Ir_{0.91}Co_{0.09})_4Sn_{13}$ (solid circles) in comparison to $Ca_3Ir_4Sn_{13}$ (open triangles). Inset: same data showing the low-temperature regime around T_c.

is shown in the inset in Fig. 4(a), which agrees well with previous reports [8]. The specific heat of $Ca_3(Ir_{0.91}Co_{0.09})_4Sn_{13}$ in the low-temperature regime is shown in Fig. 4(b); the inset

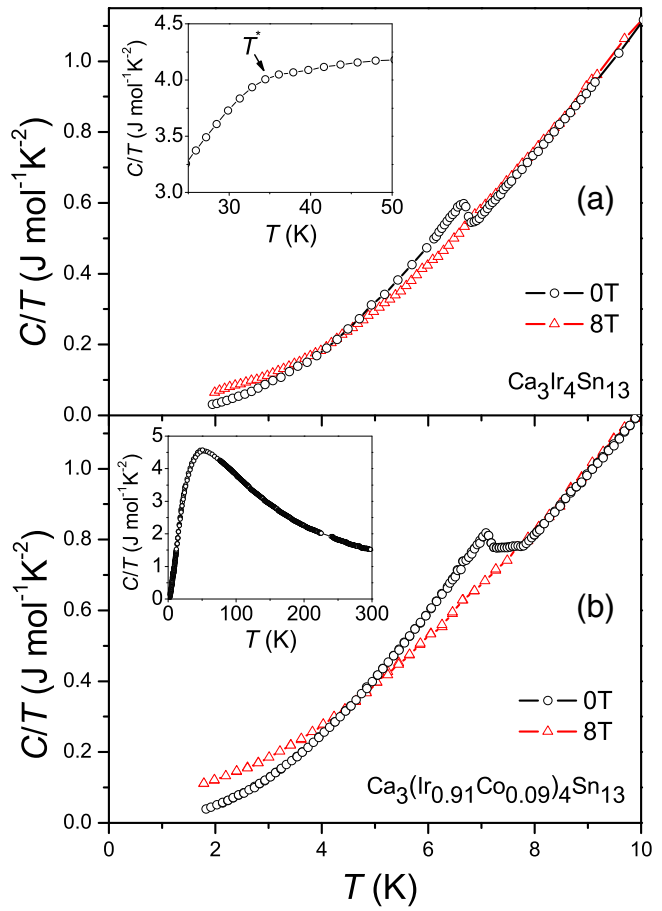

FIG. 4. Total specific heat divided by temperature vs temperature of $Ca_3Ir_4Sn_{13}$ (a) and $Ca_3(Ir_{0.91}Co_{0.09})_4Sn_{13}$ (b) in different magnetic fields. The inset in (a) shows the anomaly of $Ca_3Ir_4Sn_{13}$ at 38 K; the inset in (b) shows C/T of $Ca_3(Ir_{0.91}Co_{0.09})_4Sn_{13}$ from 0 to 300 K.

shows the entire temperature range up to 300 K. The superconducting transition temperature of $Ca_3(Ir_{0.91}Co_{0.09})_4Sn_{13}$ is $T_c = 7.3$ K, as derived from the midpoint of the specific-heat jump. At low temperature the normal-state specific heat C_n can be written according to the standard low-temperature expansion with

$$C_n(T \to 0) = \gamma_n T + \sum_{n=1}^{3} \beta_{2n+1} T^{2n+1}. \quad (1)$$

The first term is the electronic contribution, with $\gamma_n = \frac{1}{3}\pi^2 k_B^2 (1+\lambda_{ep}) N(E_F)$[$k_B$ is the Boltzmann constant, λ_{ep} is the electron-phonon coupling constant, and $N(E_F)$ is the electronic density of states at the Fermi level including two spin directions]. The second term is the low-temperature expansion of the lattice contribution, with $\beta_3 = \frac{12}{5} N_A k_B \pi^4 \Theta_D^{-3}(0)$[$N_A$ is Avogadro's number and $\Theta_D(0)$ is the initial Debye temperature]. The specific-heat data in an 8 T magnetic field represents the normal state and is suitable for calculating γ_n and β_3. The data from 1.8 to 5 K is well fitted by $C_n/T = \gamma_n + \beta_3 T^2 + \beta_5 T^4$, and we obtain $\gamma_n = 40$ mJ mol^{-1} K^{-2}, $\beta_3 = 11.9$ mJ mol^{-1} K^{-4}, and $\Theta_D(0) = 149$ K ($Ca_3Ir_4Sn_{13}$), as well as $\gamma_n = 60$ mJ mol^{-1} K^{-2}, $\beta_3 = 12.0$ mJ mol^{-1} K^{-4}, and $\Theta_D(0) = 150$ K [$Ca_3(Ir_{0.91}Co_{0.09})_4Sn_{13}$] (see Table I). The values for $Ca_3Ir_4Sn_{13}$ are in excellent agreement with Ref. [8].

The electronic specific heat can be obtained by subtracting the normal-state phonon contribution derived from the 8 T data. Figure 5 shows the electronic contribution to the specific heat C_e/T of $Ca_3Ir_4Sn_{13}$ and $Ca_3(Ir_{0.91}Co_{0.09})_4Sn_{13}$. The left inset shows the thermodynamic critical field $H_c(T)$, which is obtained by numerical integration of the electronic specific-heat component:

$$-\frac{1}{2}\mu_0 V H_c^2(T) = \Delta U(T) - T\Delta S(T)$$
$$= \int_T^{T_c} [C_s(T') - C_n(T')] dT'$$
$$- T \int_T^{T_c} \frac{C_s(T') - C_n(T')}{T'} dT',$$

TABLE I. Characteristic parameters of $Ca_3(Ir_{0.91}Co_{0.09})_4Sn_{13}$ in comparison to $Ca_3Ir_4Sn_{13}$. T_c: superconducting transition temperature from the specific heat; γ_n: normal-state Sommerfeld coefficient; $\Delta C/T_c$: specific-heat jump at T_c; $\Delta C/\gamma_n T_c$: normalized specific-heat jump; $\Theta_D(0)$: initial Debye temperature; $H_c(0)$: thermodynamic critical field at $T = 0$ derived from the specific heat; $2\Delta_0/k_B T_c$: normalized superconducting gap value.

	$Ca_3(Ir_{0.91}Co_{0.09})_4Sn_{13}$	$Ca_3Ir_4Sn_{13}$
T_c (K) specific heat	7.3	6.8
γ_n(mJ/mol^{-1} K^{-2})	60	40 (41[a])
$\Delta C/T_c$(mJ/mol^{-1} K^{-2})	160	100 (114.0[a])
$\Delta C/\gamma_n T_c$	2.7	2.5 (2.78[a])
$\Theta_D(0)$(K)	150	149 (149.5[a])
$H_c(0)$(mT)	99	78
$2\Delta_0/k_B T_c$	4.9	4.5

[a]Reference [8].

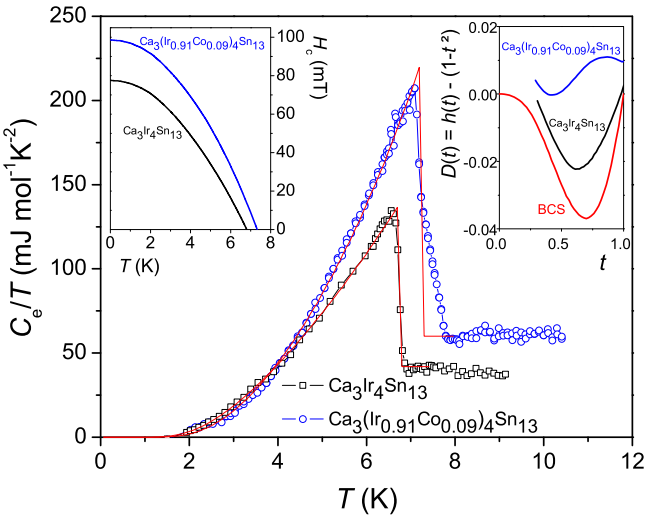

FIG. 5. Electronic contribution to the specific heat C_e/T of $Ca_3Ir_4Sn_{13}$ and $Ca_3(Ir_{0.91}Co_{0.09})_4Sn_{13}$. The phonon contribution was separated using the low-temperature expansion of the specific heat as obtained from a fit to the normal-state data in an 8 T magnetic field. The additional lines are fits with a BCS s-wave single-band α model of superconductivity [22] with sole parameter $\alpha = 2\Delta_0/k_BT_c = 4.5$ and $\alpha = 2\Delta_0/k_BT_c = 4.9$ for $Ca_3Ir_4Sn_{13}$ and $Ca_3(Ir_{0.91}Co_{0.09})_4Sn_{13}$, respectively. The left inset shows the thermodynamic critical field $H_c(T)$ of $Ca_3Ir_4Sn_{13}$ and $Ca_3(Ir_{0.91}Co_{0.09})_4Sn_{13}$ as derived from integration of the specific-heat data. The right inset shows the deviation function of the thermodynamic critical fields for both samples in comparison to the BCS weak-coupling limit (see text for details).

where the volume V and other specific quantities refer to one mole. For both samples $H_c(T)$ is nearly parabolic and extrapolates to 78 and 99 mT at $T = 0$ for $Ca_3Ir_4Sn_{13}$ and $Ca_3(Ir_{0.91}Co_{0.09})_4Sn_{13}$, respectively (Table I). The deviation function $D(t) \equiv h - (1 - t^2)$, where $h \equiv H_c(T)/H_c(0)$ and $t \equiv T/T_c$, is considered to be an indicator of the superconducting coupling strength [21]. The curves for both materials (right inset of Fig. 5) deviate clearly from the BCS predictions with a stronger deviation for $Ca_3(Ir_{0.91}Co_{0.09})_4Sn_{13}$. This provides evidence for strong-coupling superconductivity in both materials, with a slightly enhanced coupling strength in $Ca_3(Ir_{0.91}Co_{0.09})_4Sn_{13}$, which is also reflected in its higher T_c value. This is in line with other indications of the coupling strength from the normalized specific-heat jump at T_c or a fit of the α model [22] as shown in the following. At the superconducting transition temperature, the specific-heat jumps are $\Delta C/T_c = 100\,\mathrm{mJ\,mol^{-1}\,K^{-2}}$ and $\Delta C/\gamma_n T_c = 2.5$ ($Ca_3Ir_4Sn_{13}$), as well as $\Delta C/T_c = 160\,\mathrm{mJ\,mol^{-1}\,K^{-2}}$ and $\Delta C/\gamma_n T_c = 2.7$ [$(Ca_3(Ir_{0.91}Co_{0.09})_4Sn_{13}$], which are both much larger than the BCS value 1.43 and thus further confirm the strong-coupling superconductivity in both samples. Note that our value of $\Delta C/\gamma_n T_c = 2.5$ for $Ca_3Ir_4Sn_{13}$ is somewhat smaller than in Ref. [8] ($\Delta C/\gamma_n T_c = 2.78$), which is mainly because of their determination of ΔC from an extrapolation to the onset T_c value. We feel that it is better justified to determine this value at the midpoint of the specific-heat jump.

The electronic specific heat C_e contains two contributions: C_{es} (superconducting state) and C_{en} (normal state), which can be written as

$$\frac{C_{es}}{T} = \frac{4N(0)}{k_BT}\int_0^{\hbar\omega_D} d\varepsilon\left[\varepsilon^2 + \Delta^2 - \frac{T}{2}\frac{d\Delta^2}{dT}\right] \times (1 + e^{E/k_BT})^{-2}e^{E/k_BT}, \quad T \leqslant T_c$$

$$\frac{C_{en}}{T} = \gamma_n, \quad T > T_c,$$

where $E = \sqrt{\varepsilon^2 + \Delta^2}$, $\Delta(T)$ is the gap function at finite temperatures, and ω_D is the Debye frequency. The additional lines in Fig. 5 are fits according to the single-band s-wave α model of superconductivity with sole parameter $\alpha = 2\Delta(0)/k_BT_c = 4.5 \pm 0.1$ ($Ca_3Ir_4Sn_{13}$) and $2\Delta(0)/k_BT_c = 4.9 \pm 0.1$ [$Ca_3(Ir_{0.91}Co_{0.09})_4Sn_{13}$], which was adapted from the Bardeen-Cooper-Schrieffer theory [22]. All these parameters thus consistently confirm a strong-coupling superconductivity in both materials, with a slightly enhanced coupling strength in $Ca_3(Ir_{0.91}Co_{0.09})_4Sn_{13}$. The latter is also reflected in its higher T_c value. A detailed table with all parameters derived from the specific heat is presented in Table I.

The superconducting specific-heat transition is slightly broadened, which may be associated to some inhomogeneity of the Co content. However, this is not expected to influence the following analysis of the normal-state properties significantly. Note that we use the Co substitution here as a tool to suppress the T^* anomaly entirely, which will allow us to extract the phonon density of states and the electron-phonon coupling strength from specific heat and resistivity, respectively. This is not possible with sufficient accuracy in the presence of the T^* anomaly.

IV. PHONON DENSITY OF STATES AND ELECTRON-PHONON COUPLING STRENGTH

To understand the origin of superconductivity of $Ca_3(Ir_{0.91}Co_{0.09})_4Sn_{13}$, it is desirable to investigate the phonon density of states in detail and the coupling of the phonon modes to the electrons. In order to obtain the phonon density of states (PDOS) $F(\omega)$ from the specific-heat data, we use a deconvolution of the normal-state specific-heat data into a set of Einstein modes with fixed spacing on a logarithmic frequency scale with adjustable weights [23–26].

$$F(\omega) = \sum_k F_k\delta(\omega - \omega_k). \tag{2}$$

The corresponding lattice specific heat is given by

$$C_{ph}(T) = 3N_Ak_B\sum_k F_k\frac{x_k^2e^{x_k}}{(e^{x_k} - 1)^2}, \tag{3}$$

where $x_k = \omega_k/T$. The weights F_k are determined by using least-square fits to the lattice specific heat. This model is valid for the entire temperature range, in contrast to the low-temperature expansion based on the above approximation we used to describe the lattice specific heat in the vicinity of the superconducting transition, previously. The Einstein modes are chosen as $\omega_{k+1}/\omega_k = 1.75$, which is small enough to get a rough fingerprint of the phonon density of states. The aim of this deconvolution is not to find the exact energy of each mode, but to establish a histogram of the density of states in

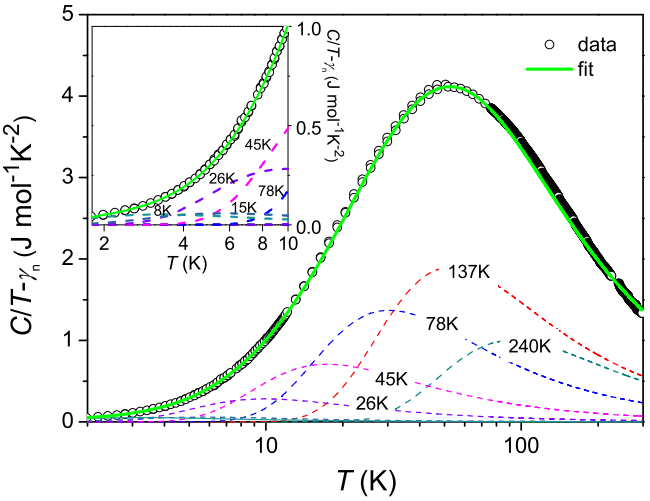

FIG. 6. Lattice specific heat divided by temperature of $Ca_3(Ir_{0.91}Co_{0.09})_4Sn_{13}$ showing the decomposition into Einstein terms on a logarithmic temperature scale. The labels correspond to Einstein temperatures $\Theta_{E,k}$. A set of Einstein terms with $\Theta_{E,k} =$ 8,15,26,45 K,78,137, and 240 K is sufficient to obtain a good fit to the lattice specific heat. The inset show details below 10 K.

predefined frequency bins. Figure 6 shows the specific heat of $Ca_3(Ir_{0.91}Co_{0.09})_4Sn_{13}$ and its decomposition into 11 Einstein modes. The PDOS obtained in this way is shown in Fig. 7. A peak unveils at the mode of 12 meV, which indicates that this mode contributes significantly to the lattice specific heat. To determine whether or not this mode strongly contributes to the electron-phonon coupling, and thus likely plays a role for the Cooper-pairing mechanism, we use in the following the resistivity as a probe to study the electron-phonon coupling strength of the different modes.

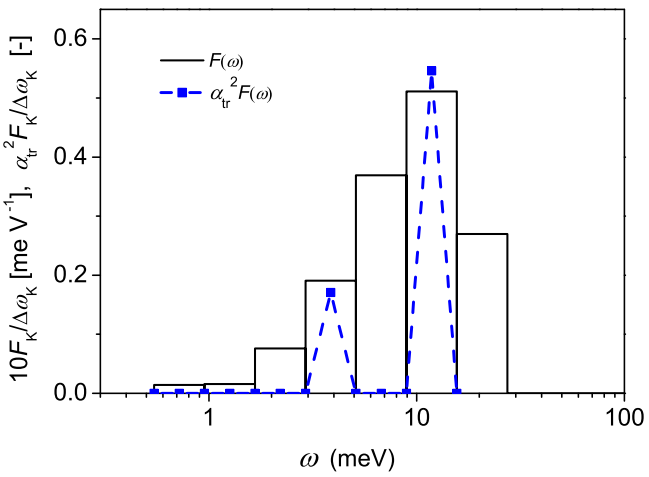

FIG. 7. Phonon density of states $F(\omega)$ deconvolved from the specific heat and electron-phonon transport coupling function $a_{tr}{}^2F(\omega)$ deconvolved from the resistivity of $Ca_3(Ir_{0.91}Co_{0.09})_4Sn_{13}$. Fits are performed with δ functions $F_k\delta(\omega-\omega_k)$ and $(a_{tr}{}^2F)_k\delta(\omega-\omega_k)$ on a basis of Einstein frequencies $\omega_{k+1} = 1.75\omega_k$. In order to reflect the spectral density, the δ functions of the PDOS are represented by a histogram of width $\Delta\omega_k = 1.75^{1/2}\omega_k - \omega_k/1.75^{1/2}$ with height $F_k/\Delta\omega_k$ and $(a_{tr}{}^2F)_k/\Delta\omega_k$.

The resistivity of $Ca_3(Ir_{0.91}Co_{0.09})_4Sn_{13}$ is analyzed in a similar way. The temperature-dependent electrical resistivity $\rho(T)$ in a nonmagnetic metallic crystalline solid is given by the Bloch-Grüneisen formula [27]:

$$\rho_{BG}(T) = \rho(0) + \frac{4\pi m^*}{ne^2}\int_0^{\omega_{\max}} \alpha_{tr}^2F(\omega)\frac{xe^x}{(e^x-1)^2}d\omega, \quad (4)$$

where $x \equiv \omega/T$ and $a_{tr}{}^2F(\omega)$ is the electron-phonon "transport coupling function." A deconvolution method is used to decompose the resistivity into Bloch-Grüneisen modes, which includes adjustable weights similar to Eq. (2):

$$\alpha_{tr}^2F(\omega) = \frac{1}{2}\sum_k \lambda_{tr,k}\omega_k\delta(\omega-\omega_k) \quad (5)$$

and in this way a decomposed resistivity function [26] is obtained:

$$\rho_{BG}(T) = \rho(0) + \frac{2\pi}{\varepsilon_0\Omega_p^2}\sum_k \lambda_{tr,k}\omega_k\frac{x_ke^{x_k}}{(e^{x_k}-1)^2}, \quad (6)$$

where the fitting parameters are the dimensionless constraints $\lambda_{tr,k}$ with restrictions $\lambda_{tr,k} \geqslant 0$. $\Omega_p \equiv (ne^2/\varepsilon_0m^*)^{1/2}$ is the unscreened plasma frequency. In this analysis, the exact value of $\lambda_{tr} = \sum_k \lambda_{tr,k}$ is unknown, so the relative weight in our fitting $\lambda_{tr,k}$ is in arbitrary units to illustrate the electron-phonon coupling strength of the different modes. To minimize the number of fitting parameters, the same set of phonon frequencies is used as in the fit to the specific heat. At room temperature, the resistivity of $Ca_3(Ir_{0.91}Co_{0.09})_4Sn_{13}$ is about 80 $\mu\Omega$ cm. The data exhibits a negative curvature in the high-temperature regime above ~120 K. This is a rather general phenomenon, which occurs, for example, when the Mott limit [28–30] is reached, and therefore an empirical "parallel-resistor" formula [31] is included in our analysis:

$$\frac{1}{\rho(T)} = \frac{1}{\rho_{\text{ideal}}(T)} + \frac{1}{\rho_{\max}}, \quad (7)$$

where $\rho_{\max} = 122\,\mu\Omega$ cm is the maximum resistivity, which is fitted simultaneously with the parameters $\lambda_{tr,k}$. Note that this procedure is purely phenomenological and only used "cosmetically" to account for the saturating behavior of the resistivity without knowing its exact origin. It does not have a strong influence on the fitting result, for which the initial upturn of the resistivity in the temperature range below 75 K is most sensitive, where the saturation effect is not yet significant. We tried the fitting by limiting the temperature range to 100 and 200 K, but the result was qualitatively similar to the behavior obtained from fits over the entire temperature range up to 300 K. This is because the resistive behavior appears to be dominated by only two low-energy modes, and the corresponding Bloch-Grüneisen functions already approach a linear behavior above 75 K, as we will demonstrate in the following.

Figure 8 shows the resistivity vs temperature and its decomposition into 11 Bloch-Grüneisen modes. The corresponding electron-phonon transport coupling function $a_{tr}{}^2F(\omega)$ is included in Fig. 7 for comparison with the phonon density of states. The deconvolution of the resistivity yields a good representation of the phonon peak at 12 meV obtained from the deconvolution of the specific heat. Only two frequency modes stand out in the resistivity fitting and the mode at 12 meV

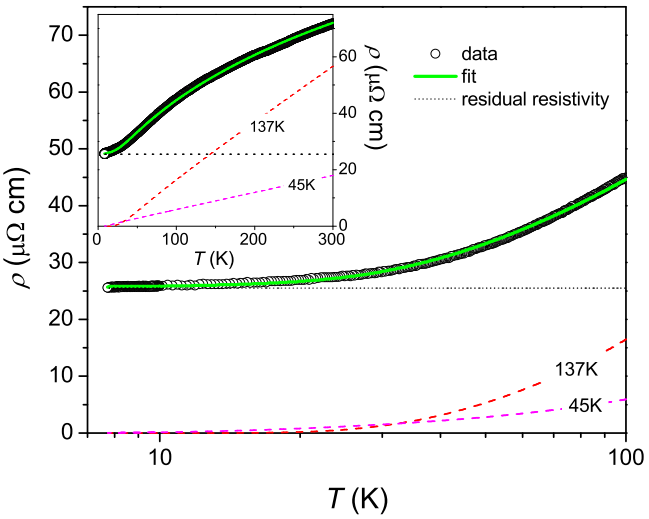

FIG. 8. Total resistivity of $Ca_3(Ir_{0.91}Co_{0.09})_4Sn_{13}$ on a logarithmic temperature scale showing the decomposition into Bloch-Grüneisen terms and the residual resistivity term (horizontal dotted line). The labels k correspond to Einstein temperatures $\Theta_{E,k}$. A set of only two Bloch-Grüneisen terms with $\Theta_{E,k} = 45$ and 137 K is sufficient to obtain a good fit to the resistivity (see text for details). The inset shows the entire temperature range on a linear scale.

dominates the electron-phonon transport function, which is in accordance with the peak in the PDOS and illustrates that this phonon mode is strongly coupled to the electrons. Compared with previous research on electron-phonon coupling [23–26,32], it is indeed rational to explain a superconducting transition temperature of 7 K with a phonon energy of 12 meV. Therefore, we can conclude that the phonon mode at ∼12 meV (or a group of soft phonon modes in a narrow range around this frequency, which cannot be resolved individually by our deconvolution technique) plays an important role for the superconductivity in $Ca_3(Ir_{0.91}Co_{0.09})_4Sn_{13}$. This makes a spin-fluctuation-mediated Cooper-pairing scenario unlikely and rather points out a conventional phonon-mediated superconducting pairing mechanism. The group of phonons that appear to mediate superconductivity occurs thus at significantly higher energy than the breathing mode of the Sn_{12} icosahedra believed to drive the structural instability at T^* [13].

Our results cannot distinguish whether the changes in the lattice dynamics are driven by the charge fluctuations or whether the changes in the electronic spectrum at much higher energies are the result of an instability of the chemical structure. Our results suggest that the softening of the breathing mode causes a redistribution of spectral weight at higher phonon energies, which depends on Co content and is reflected in the higher superconducting transition temperature and slightly larger superconducting coupling strength of $Ca_3(Ir_{0.91}Co_{0.09})_4Sn_{13}$ compared to $Ca_3Ir_4Sn_{13}$.

V. CONCLUSION

In summary, we report specific heat and resistivity data of a Co-substituted $Ca_3(Ir_{0.91}Co_{0.09})_4Sn_{13}$ sample in comparison to $Ca_3Ir_4Sn_{13}$, for which the structural instability at T^* observed in the stoichiometric compound $Ca_3Ir_4Sn_{13}$ is completely suppressed. The superconducting transition temperature of $Ca_3(Ir_{0.91}Co_{0.09})_4Sn_{13}$ is 7.3 K, which is slightly higher than the $T_c = 6.8$ K of $Ca_3Ir_4Sn_{13}$. The specific heat of both $Ca_3Ir_4Sn_{13}$ and $Ca_3(Ir_{0.91}Co_{0.09})_4Sn_{13}$ in the superconducting state is characteristic for a single-band isotropic BCS superconductor with strong electron-phonon coupling, with $Ca_3Ir_4Sn_{13}$ having a slightly enhanced coupling strength with respect to $Ca_3Ir_4Sn_{13}$ (in agreement with its higher T_c value). To obtain the phonon density of states $F(\omega)$ and the spectral electron-phonon coupling function ${a_{tr}}^2F(\omega)$, a deconvolution technique was applied to the specific-heat and resistivity data of $Ca_3(Ir_{0.91}Co_{0.09})_4Sn_{13}$. In this way, we established histograms of the phonon density of states and the electron-phonon coupling constant in predefined frequency bins. Both contain a pronounced peak at 12 meV. The comparative analysis of specific-heat and resistivity data thus confirms that a narrow group of phonon modes around 12 meV, which are strongly coupled to the electrons, plays an important role in the superconducting mechanism of $Ca_3(Ir_{0.91}Co_{0.09})_4Sn_{13}$. Our results cannot clarify the role of the charge-density-wave instability for superconductivity, but they clearly demonstrate the importance of phonons in the strong-coupling superconducting mechanism in this class of materials.

ACKNOWLEDGMENTS

The research leading to these results has received funding from the Research Grants Council of Hong Kong Grants No. SEGHKUST03 and No. 603010, as well as from the European Community's Seventh Framework Programme (FP7/2007-2013) under grant agreement No. 290605 (COFUND: PSIFELLOW).

[1] M. R. Norman, Science **332**, 196 (2011).
[2] G. R. Stewart, Z. Fisk, J. O. Willis, and J. L. Smith, Phys. Rev. Lett. **52**, 679 (1984).
[3] N. D. Mathur, F. M. Grosche, S. R. Julian, I. R. Walker, D. M. Freye, R. K. W. Haselwimmer, and G. G. Lonzarich, Nature (London) **394**, 39 (1998).
[4] C. C. Tsuei and J. R. Kirtley, Rev. Mod. Phys. **72**, 969 (2000).
[5] K. An, T. Sakakibara, R. Settai, Y. Onuki, M. Hiragi, M. Ichioka, and K. Machida, Phys. Rev. Lett. **104**, 037002 (2010).
[6] A. P. Mackenzie and Y. Maeno, Rev. Mod. Phys. **75**, 657 (2003).
[7] E. Morosan, H. W. Zandbergen, B. S. Dennis, J. W. G. Bos, Y. Onose, T. Klimczuk, A. P. Ramirez, N. P. Ong, and R. J. Cava, Nat. Phys. **2**, 544 (2006).
[8] J. Yang, B. Chen, C. Michioka, and K. Yoshimura, J. Phys. Soc. Jpn. **79**, 113705 (2010).
[9] S. Gerber, J. L. Gavilano, M. Medarde, V. Pomjakushin, C. Baines, E. Pomjakushina, K. Conder, and M. Kenzelmann, Phys. Rev. B **88**, 104505 (2013).
[10] J. Remeika, G. Espinosa, A. Cooper, H. Barz, J. Rowell, D. McWhan, J. Vandenberg, D. Moncton, Z. Fisk, L. Woolf, H.

Hamaker, M. Maple, G. Shirane, and W. Thomlinson, Solid State Commun. **34**, 923 (1980).
[11] G. Espinosa, Mater. Res. Bull. **15**, 791 (1980).
[12] L. E. Klintberg, S. K. Goh, P. L. Alireza, P. J. Saines, D. A. Tompsett, P. W. Logg, J. Yang, B. Chen, K. Yoshimura, and F. M. Grosche, Phys. Rev. Lett. **109**, 237008 (2012).
[13] D. G. Mazzone, S. Gerber, J. L. Gavilano, R. Sibille, M. Medarde, B. Delley, M. Ramakrishnan, M. Neugebauer, L. P. Regnault, D. Chernyshov, A. Piovano, T. M. Fernández-Díaz, L. Keller, A. Cervellino, E. Pomjakushina, K. Conder, and M. Kenzelmann, Phys. Rev. B **92**, 024101 (2015).
[14] K. Wang and C. Petrovic, Phys. Rev. B **86**, 024522 (2012).
[15] L. M. Wang, C.-Y. Wang, G.-M. Chen, C. N. Kuo, and C. S. Lue, New J. Phys. **17**, 033005 (2015).
[16] S. Y. Zhou, H. Zhang, X. C. Hong, B. Y. Pan, X. Qiu, W. N. Dong, X. L. Li, and S. Y. Li, Phys. Rev. B **86**, 064504 (2012).
[17] A. F. Fang, X. B. Wang, P. Zheng, and N. L. Wang, Phys. Rev. B **90**, 035115 (2014).
[18] M. Ramakrishnan, Master's thesis, ETH Zürich, 2013.
[19] P. K. Biswas, Z. Guguchia, R. Khasanov, M. Chinotti, L. Li, K. Wang, C. Petrovic, and E. Morenzoni, Phys. Rev. B **92**, 195122 (2015).
[20] W. C. Yu, Y. W. Cheung, P. J. Saines, M. Imai, T. Matsumoto, C. Michioka, K.Yoshimura, and S. K. Goh, Phys. Rev. Lett. **115**, 207003 (2015).
[21] J. P. Carbotte, Rev. Mod. Phys. **62**, 1027 (1990).
[22] H. Padamsee, J. E. Neighbor, and C. A. Shiffman, J. Low Temp. Phys. **12**, 387 (1973).
[23] R. Lortz, Y. Wang, U. Tutsch, S. Abe, C. Meingast, P. Popovich, W. Knafo, N. Shitsevalova, Y. B. Paderno, and A. Junod, Phys. Rev. B **73**, 024512 (2006).
[24] R. Lortz, R. Viennois, A. Petrovic, Y. Wang, P. Toulemonde, C. Meingast, M. M. Koza, H. Mutka, A. Bossak, and A. San Miguel, Phys. Rev. B **77**, 224507 (2008).
[25] J. Teyssier, R. Lortz, A. Petrovic, D. van der Marel, V. Filippov, and N. Shitsevalova, Phys. Rev. B **78**, 134504 (2008).
[26] R. Lortz, Y. Wang, S. Abe, C. Meingast, Y. B. Paderno, V. Filippov, and A. Junod, Phys. Rev. B **72**, 024547 (2005).
[27] G. Grimvall, in *The Electron-Phonon Interaction in Metals*, Selected Topics in Solid State Physics, edited by E. Wohlfarth (Elsevier, North-Holland, New York, 1981).
[28] N. E. Hussey, K. Takenaka, and H. Takagi, Philos. Mag. **84**, 2847 (2004).
[29] N. F. Mott, Adv. Phys. **16**, 49 (1967).
[30] S. N. Mott, Rev. Mod. Phys. **50**, 203 (1978).
[31] H. Wiesmann, M. Gurvitch, H. Lutz, A. Ghosh, B. Schwarz, M. Strongin, P. B. Allen, and J. W. Halley, Phys. Rev. Lett. **38**, 782 (1977).
[32] D. A. Tompsett, Phys. Rev. B **89**, 075117 (2014).